PIB: Parallel ion beam etching of sections collected on wafer for ultra large-scale connectomics

Authors: Hongtu Ma [1]†, Yanan Lv[1,2]†, Minggang Wang[1]†, Zhuangzhuang Zhao[1,2]†, Jing Liu[1]†, Xiaohui Dong[1], Yanchao Zhang[1,2], Jinyue Guo[1,2], Bohao Chen[1,2], Lina Zhang[1], Sheng Chang[1], Haoran Chen[1,2], Hao Zhai[1], Linlin Li[1*], Xi Chen[1*], Hua Han[1,2*]

Affiliations:

[1] State Key Laboratory of Brain Cognition and Brain-inspired Intelligence Technology, Institute of Automation, Chinese Academy of Sciences, Beijing, China.

[2]School of Future Technology, School of Artificial Intelligence, University of Chinese Academy of Sciences, Beijing, China.

*Corresponding authors. Email: hua.han@ia.ac.cn (Hua Han); xi.chen@ia.ac.cn (Xi Chen); lilinlin@ia.ac.cn (Linlin Li).

†These authors contributed equally to this work.

Abstract: We have developed a parallel ion beam etching device enabling simultaneous 20 nm thickness reduction for hundreds of biological sections, which could be collected on a whole 4-inch wafer. Through cyclic scanning electron microscopy imaging and ion beam thinning, it is trustworthy and efficient to obtain three-dimensional volume with high axial resolution for millimeter-size samples compared to conventional volume electron microscopy methods.

Introduction

High-resolution volume electron microscopy (vEM) imaging of biological samples is critical in connectomics, where the goal is to map neural circuits in unprecedented detail [1-3]. As this field progresses, efforts to achieve high-resolution imaging of large-scale brain samples, have become a priority for future connectomics research [4]. Traditional vEM methods for large specimens rely heavily on ultramicrotomes to produce thousands of ultrathin serial sections [5-8]. However, these methods are limited in terms of achievable axial resolution, as the precision of section thickness is restricted by the mechanical limits of ultramicrotomes, particularly in maintaining stable operation over extended periods [9]. Additionally, the ultrathin sectioning process is highly sensitive to environmental factors such as vibrations and temperature fluctuations, which frequently result in sectioning failures and lower throughput [10]. Consequently, the axial resolution for section-based vEM methods typically exceeds 30 nm, hindering the detailed analysis of neuronal connections, and reducing the accuracy of automatic 3D segmentation and the efficiency of manual proofreading. In contrast to the limited processing area of Focused Ion Beam Scanning Electron Microscopy (FIB-SEM), Gas Cluster Ion Beam Scanning Electron Microscopy (GCIB-SEM) can achieve high axial resolution while thinning samples over a 7x7 mm^2 area at one operation process [11, 12]. This capability allows for the processing of larger samples, yet for whole mouse brains, the efficiency of thinning several sections simultaneously still falls short of the demands for high-throughput imaging. To address these challenges, we develop a section-thinning device that employs parallel ion beam etching (PIB) technology, adapted from the semiconductor field. By reducing incident energy of the

ion beam, the device can effectively process sections collected on a whole 4-inch wafer simultaneously with 20nm thinning step. This advancement addresses the axial resolution requirements for ultra large brain samples and significantly enhances the efficiency, scalability and robustness of sample preparation in connectomics, facilitating the study of larger brain regions with higher accuracy and reliability.

In GCIB-SEM, the beam diameter is approximately 250 μm, which necessitates the use of an electrostatic scanning plate to enable rapid deflection of the ion beam across the sample surface [12]. This limitation constrains the effective processing area to less than 10 mm. Moreover, to minimize thinning artifacts, the ion beam is typically incident at an angle of 30 degrees, which can lead to uneven thinning across larger samples. This non-uniformity needs additional post-processing steps to achieve the flatness of the imaged 3D volume. In contrast, our method generates a parallel ion beam that delivers uniform energy across a much larger area of up to 150 mm. This capability enables consistent thinning of hundreds of sections collected on a 4-inch wafer simultaneously, which is desirable for high-throughput electron microscopy imaging. Furthermore, the PIB method employs a shallower incident angle of 5 degrees, significantly mitigating the impact of differential sputtering efficiency associated with varying atomic numbers in the sample. This design feature contributes to a more uniform thinning process, enhancing the overall quality and consistency of sample preparation in connectomics research.

Our PIB prototype device includes control system, vacuum system, RF power supply, ion source, neutralizer, and thinning chamber (Supplementary Fig. 1a, b, c). In contrast to ion guns such as FIB and GCIB, PIB generates a parallel ion beam with a diameter of up to 150 mm. This capability is enabled by the triple-grid regulation mechanism of the ion source (Fig. 1a, b, c; Supplementary Fig. 2a). In this design, the acceleration and ground grids primarily collimate the ion beam without changing its kinetic energy, while the beam energy is determined by the voltage applied to the screen grid (Supplementary Fig. 2b). The neutralizer emits low-energy electrons to compensate for the positive charges within the ion beam, thereby suppressing beam divergence and preventing charge accumulation on the sample surface. The relatively low energy and parallelism of the ion beam are essential for achieving uniform, large-area 20nm thinning of biological sections at one time (see *Methods* for working principle of ion source).

The workflow of PIB-SEM is illustrated in Fig. 1d. The sample is cut into serial sections with a thickness of about 100 nm using ultramicrotome. Compared to 30 nm sections, it is much easier to obtain qualified continuous sections with 100 nm thickness, which are free of distortion, such as wrinkle and tear. The ribbons of serial sections are then collected on hydrophilized silicon (Si) pieces. After imaging the region of interest of serial sections in SEM, these Si pieces are mounted in PIB to remove the surface of the sections with a thickness of 20 nm. Through multiple imaging and thinning cycles, we obtain EM images of all sections with a 20 nm axial resolution. Finally, the obtained image stack is aligned to generate the 3D volume of the sample.

Results

To evaluate the performance of PIB-SEM for high-resolution volumetric imaging, we use the sample from prefrontal cortex of a rat (see *Methods* for prefrontal cortex of rat). A total of 1018 consecutive sections with 100 nm thickness are obtained and collected on three hydrophilized Si pieces (Supplementary Fig. 4b). After imaging in Zeiss Gemini SEM 300 with aBSD detector, these Si pieces are individually placed into the thinning chamber of PIB to remove the surface of the sections,

which take about 12 min to thinning 20nm. Due to mechanical deviations of the ultramicrotome, we perform multiple cycles of imaging and thinning, with the number of cycles depending on the thickness of the thickest section. For those thinner sections, the images obtained in the last few cycles have no meaningful content, so we discard them in serial sections alignment (Supplementary Fig. 5). Two consecutive sections with 5 different thinning cycles are shown in Fig. 1e, where the continuity of neural substructures within and between sections are preserved. All sections are stitched into a volume of 83 μm × 83 μm × 101 μm. A sub-volume of 4 μm × 4 μm × 2 μm spanning 20 sections (Fig. 1f) and a sub-volume of 8 μm × 8 μm × 4 μm spanning 40 sections (Supplementary Fig. 6, Supplementary Video 1) are presented in detail.

To objectively evaluate the axial continuity of the PIB-SEM volume, we select the automated tape collection ultramicrotome SEM (ATUM-SEM) dataset (3 nm × 3 nm × 30 nm) [13] for comparison. The neuronal membrane structures in the PIB-SEM volume exhibit better continuity and are more easily identifiable across all three views compared to the ATUM-SEM volume. In both the XZ and YZ views, synaptic vesicles are clearly distinguishable in the PIB-SEM volume, while they appear blurry in the ATUM-SEM volume (Supplementary Fig. 7a). We quantify z-axial continuity using the Chunked Pearson Correlation Coefficient (CPC) [14] and the Structural Similarity Index Measure (SSIM) [15] (see *methods* for CPC and SSIM as continuity indicators). The PIB-SEM volume shows a 48.2% improvement in CPC and a 76.3% improvement in SSIM over the ATUM-SEM volume (Supplementary Fig. 7b), indicating better axial continuity.

As a result of superior axial resolution volumes generated by PIB-SEM, more efficient and accurate automated neuron segmentation could be achieved. The remarkable structural continuity across sections of the PIB-SEM volume facilitates seamless integration with existing general-purpose segmentation models, enabling the formation of an efficient human-in-the-loop segmentation pipeline with minimal human proofreading effort (Fig. 2a). Initially, we predict the membrane of the PIB-SEM volume using the original SegNeuron model [16], which demonstrates exceptional zero-shot performance. Experts then refine the precomputed results to establish the ground truth for model fine-tuning. Using the fine-tuned model, we performed watershed-based dense reconstruction of a 10 μm × 10 μm × 10 μm sub-volume (Supplementary Fig. 8). The finest substructures (dendritic spines and axons) can be well reconstructed (Fig. 2b), ensuring the applicability of connectomics. The superior axial resolution of PIB-SEM volume also enables more reliable connectome reconstruction. In contrast to the full resolution, the volume down-sampled to 40 nm along axial direction exhibits substantial merge or split errors, affecting the ultra-structures like spine necks and axons (Fig. 2c). These errors necessitate extensive manual proofreading, significantly increasing the labor costs for accurate connectome acquisition. These results demonstrate that the enhanced z-axis resolution of PIB preserves critical structural information essential for automated methods to achieve reliable segmentation performance.

To demonstrate the applicability of PIB-SEM for millimeter-size samples, we section the rat cortex (see *Methods* for cortex of rat spanning all cortical layers), collect 150 serial sections with 100 nm thickness (Supplementary Fig. 9a). Five PIB-SEM cycles (10 × 10 × 20 nm^3 voxels) are performed (Supplementary Fig. 9b). A volume of 1721 μm × 550 μm × 15 μm is reconstructed (Supplementary Fig. 9d), which spans all cortical layers (L1–L6) of the rat cerebral cortex. We can see the processing uniformity along the cortical layers (Supplementary Video 2).

Discussion

In summary, the two volumetric datasets acquired using PIB-SEM method demonstrate the significant potential of this technique for large-scale connectomics. Compared to conventional methods using ultramicrotome, PIB-SEM provides high axial resolution, allowing for reconstruction of more accurate structural details and substantially enhancing the performance of automated segmentation algorithms. This is crucial for dense reconstruction in large-scale vEM, as it not only increases processing efficiency but also significantly reduces the workload of manual proofreading. Most importantly, PIB-SEM supports large-area thinning, enabling the simultaneous processing of hundreds of sections with millimeter size. We assess the thinning uniformity of PIB across 4-inch wafer (see *Methods* for evaluation of thinning uniformity across 4-inch wafer), which shows that the averaged thickness of removed sample at the center of the wafer deviates from the preset value by less than 0.17 nm, while at the wafer edge the deviation is less than 4.29 nm. PIB is an independent device, and could work with several multi-beam SEM, greatly improving the imaging speed for large volume samples. Furthermore, due to the use of thicker section thickness, the collection of qualified continuous sections becomes much easier.

Nevertheless, PIB-SEM still presents certain limitations. Due to mechanical deviations in ultramicrotome, the thickness of different sections often varies, particularly at the beginning of the ribbon. To prevent sample loss, the initial sections of ribbon are typically cut with thinner thickness, resulting in inconsistent thinning cycles across different sections. Therefore, the development of rapid and precise section thickness measurement techniques for monitoring the thinning process will be critical to further improving the axial resolution of the PIB-SEM.

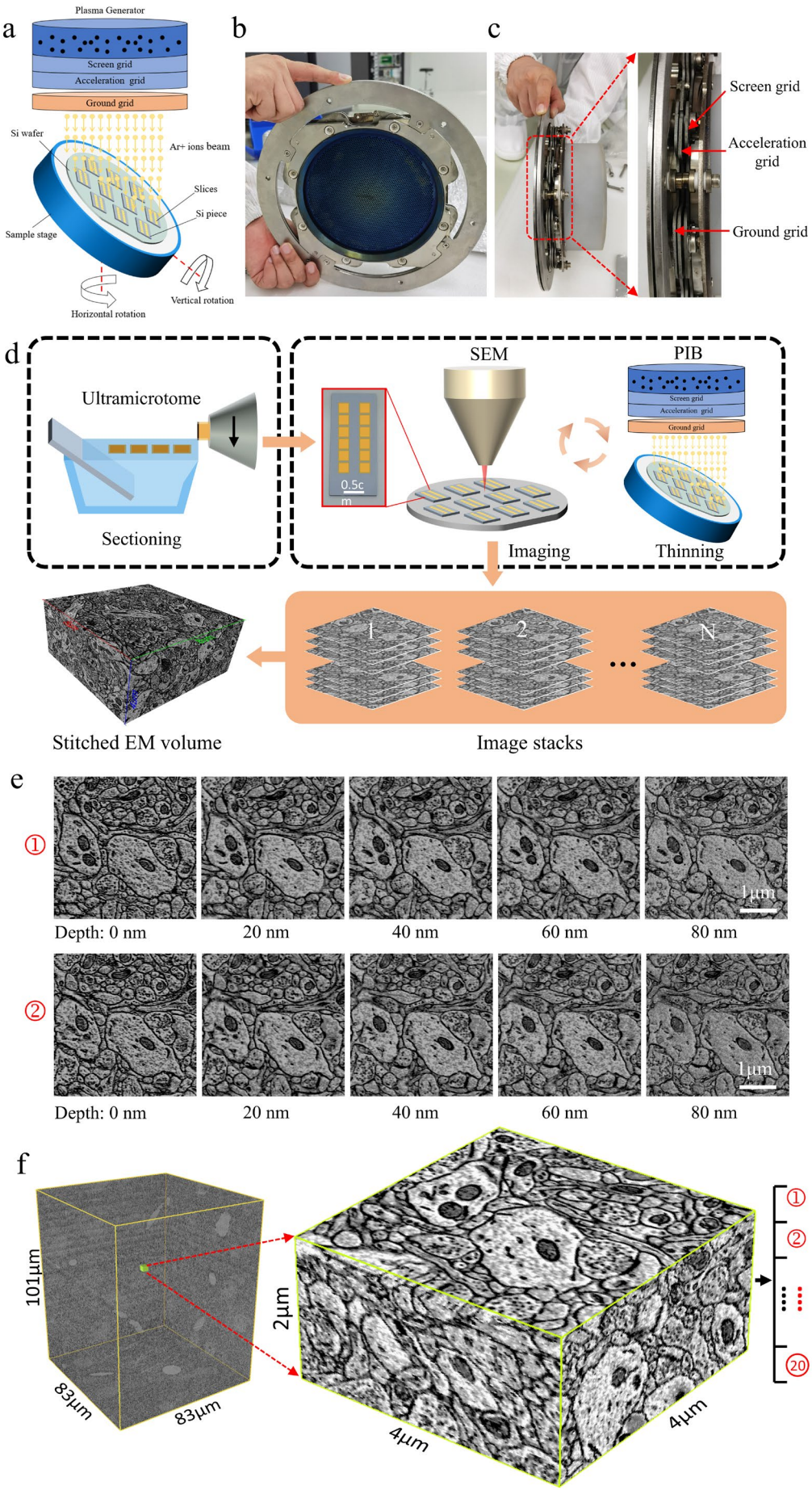
a
Plasma Generator
Screen grid
Acceleration grid
Ground grid
Si wafer
Ar+ ions beam
Slices
Si piece
Sample stage
Horizontal rotation
Vertical rotation
b
c
Screen grid
Acceleration grid
Ground grid
d
Ultramicrotome
Sectioning
SEM
PIB
Screen grid
Acceleration grid
Ground grid
0.5c
m
Imaging
Thinning
1
2
N
Stitched EM volume
Image stacks
e
①
②
Depth: 0 nm
20 nm
40 nm
60 nm
80 nm
1μm
f
101μm
83μm
83μm
2μm
4μm
4μm
①
②
⑳

Fig. 1 | PIB-SEM overview. a, Schematic diagram of PIB-SEM working principle. After the plasma is generated, it is extracted and shaped by the three-grid structure to form a large-area parallel ion beam for thinning sections. **b**, Front view of the ion source. **c,** Side view of the ion source showing the triple-grid structure, which includes the screen grid, acceleration grid, and ground grid. **d,** The workflow of PIB-SEM. First, the biological sample embedded in resin block are sliced using an ultramicrotome, and the numbered sections are collected onto silicon pieces. Next, all silicon pieces are placed into SEM for serial section imaging. After imaging, the silicon pieces are placed into the thinning chamber of PIB for section thinning, completing an PIB-SEM cycle. With several PIB-SEM cycles, we obtain the image stacks for all sections. Finally, the image stacks are aligned to form a three-dimensional volume of the biological sample. **e,** SEM images of two consecutive sections in the sub-volume at five different thinning depths. f, PIB-SEM 3D volume (83 μm × 83 μm × 101 μm) spanning 1018 sequential 100-nm sections of rat cortex, and a sub-volume (4 μm × 4 μm × 2 μm) spanning 20 sequential 100-nm sections (numbers denote individual thick sections).

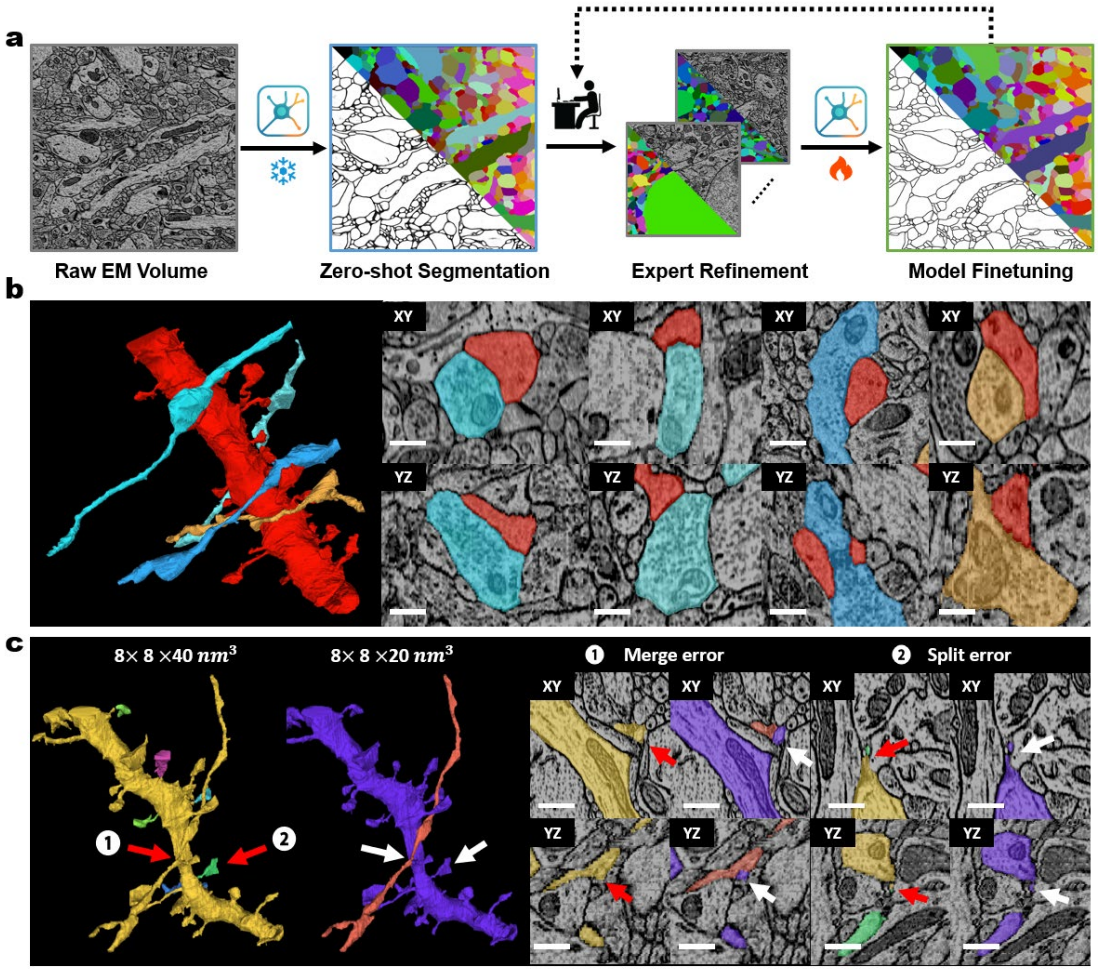

Fig. 2 | Automated segmentation of PIB-SEM data. a. Customized neural reconstruction workflow. Owing to high axial resolution and clearly defined ultrastructure in PIB-SEM volume, the general neuron segmentation model (SegNeuron) demonstrates strong reconstruction performance. Human experts only make connectivity corrections to the rough segmentation results, which are then used to fine-tune the model, further improving reconstruction accuracy. **b**. Local visualization of the neurite region, showing the connectivity between dendritic shafts and dendritic spines (scale bar: 500 nm). **c**. Comparison of segmentation model performance on the volumes with different axial resolution. The general model is fine-tuned and predicted on 40 nm and 20 nm axial resolution data. The results show that the 40 nm data introduce a large number of splitting and merging errors in finely connected regions. In contrast, the 20 nm data, thanks to its excellent spatial continuity, exhibits more accurate structural connectivity. The image on the right shows the visualization of the segmentation results on the original image (scale bar: 750 nm).

Methods

Animals

All animal experiments were conducted in accordance with the regulations of the animal care agency and the Beijing Municipal Regulations for the management of laboratory animals. The rats used in this experiment were housed in the Experimental Animal Center of Tsinghua University, adhering to the standards for experimental rat care. The facility is graded as specific pathogen-free (SPF) to ensure that the animals are in a controlled environment. The housing conditions included a 12-hour light/dark cycle, a stable temperature of 24±1°C, relative humidity of 35±4%, with water and food available ad libitum.

Samples preparation

All experimental protocols complied with relevant ethical regulations. After the rats were anesthetized with isoflurane inhalation, they underwent cardiac perfusion fixation. First, the blood was quickly flushed with 0.1 M phosphate buffer (PB). Then, a solution of 2% paraformaldehyde (PFA) and 1.25% glutaraldehyde (GA) in 0.1 M PB was quickly perfused. The perfusion of the fixative was then slowed down and continued for no longer than 20 minutes. After the perfusion, the mouse's cerebral cortex was removed. Small sample blocks, approximately 1 mm^3 in size, were trimmed from the mouse cerebral cortex and postfixed in a solution of 4% PFA and 2.5% GA in 0.1 M PB and kept at 4°C overnight. The samples were then washed using deionized water. The post-fixation was carried out with 2% OsO_4 (Ted Pella, 18451), prepared in 0.1 M PB, for a duration of 90 minutes at room temperature. Next, the samples were placed in a solution of 2.5% ferrocyanide (Sigma, 234125) in 0.1 M PB and incubated at room temperature for 90 min. Then, after washing three times with deionized water the samples were incubated in a solution of thiocarbohydrazide (TCH, Sigma, 223220) at 40°C for 45 min. After TCH treatment, the samples were thoroughly washed with deionized water and then incubated with 2% OsO_4 for 90 min. The samples were then transferred to a new centrifuge tube for washing. After that, they were incubated with 1% uranyl acetate (SPI-chem, 02624-AB) at 4°C overnight. The samples were incubated with lead aspartate solution (0.033 g lead nitrate (Sigma, 228621) dissolved in 5 mL 0.03 M aspartic acid (Sigma, 11189, pH 5.0)) at 50°C for 90 minutes. Then, the samples were dehydrated through a graded ethanol (50%, 70%, 80%, 90%, 100%, 10 min each) and pure acetone on a horizontal shaker. Subsequently, the samples were infiltrated with Epon-812 resin (SPI, Epon-812), also on a horizontal shaker. The samples were immersed in epoxy/acetone solutions with increasing epoxy concentrations: 1:1, 2:1 and 3:1, and each immersion lasted 4-8 hours. Then, pure epoxy resin was infiltrated twice under negative pressure, each immersion lasted 4-8 hours. The last step was polymerization. The samples were placed in an embedding plate and processed at 60°C for 24 hours.

Working principle of ion source

Unlike FIB and GCIB, PIB can generate a large-area uniform ion beam, thanks to the unique triple-grid regulation mechanism of the ion source (Fig. 1b, c, d; Supplementary Fig. 2b). First, in the plasma chamber of the ion source, high-energy electrons are excited by radio frequency (RF) and collided with argon gas molecules, causing ionization of the argon molecules and generating a large number of free electrons and Ar+ ions, thereby forming plasma. Then, after applying a voltage (80V) on the screen grid, Ar+ ions are extracted from the plasma chamber, while electrons are shielded

within the plasma chamber. This effectively reduces the interference of low-energy electrons on the ion beam, ensuring the purity of the ion beam. Next, the ion beam is shaped by passing through the acceleration grid (-400V), which improves the uniformity and collimation of the ion beam. The voltage of the acceleration grid needs to be precisely adjusted based on the screen grid voltage. When the acceleration grid voltage is too low, the ion beam will not be effectively collimated. Conversely, if the voltage is too high, the ion beam will be completely absorbed by the acceleration grid, preventing the ion beam from being emitted properly. Finally, the ion beam undergoes deceleration through the grounded grid, forming a low-energy ion beam. The coordination of the acceleration grid and grounded grid is mainly used for shaping the ion beam, without changing its energy, which is determined by the voltage applied to the screen grid (Supplementary Fig. 2a, b). Ultimately, the Ar+ ions are extracted and shaped by the triple-grid system, forming a parallel ion beam with a diameter of 150 mm. The ion source is purchased from Beijing SHL Company.

Sectioning

First, the Si wafer is cut into 2 cm×3 cm Si pieces using a dicing saw and cleaned and hydrophilized using a plasma cleaner. Then, an appropriate amount of water is added to the diamond knife boat (Supplementary Fig. 4a), and a thin layer of a mixture of Pattex glue (Henkel, Düsseldorf, Germany) and xylene (1:500) is applied on the side of the diamond knife that contacts the water, allowing the sections to stick together and form ribbons, thus preventing the sections from scattering. We use a room temperature diamond knife (35° angle) on an ultramicrotome (LEICA EM UC7) to slice from the rat brain embedded in Pon812 (Supplementary Fig. 4a). These sections are collected onto multiple Si pieces (Supplementary Fig. 4b; Supplementary Fig. 9a).

Prefrontal cortex of rat

The sample from prefrontal cortex of a rat was sectioned. 1018 sections with 100 nm thickness were collected on three Si pieces (Supplementary Fig. 4b). Then the Si pieces were processed in the electron irradiation device (Bio-eBeam, BEST-2000) to improve the conductivity of biological sections. After five PIB-SEM cycles were performed, these sections were almost etched away (Supplementary Fig. 4c). The PIB parameters used were as follows: ion beam energy of 80V, ion beam current of 100 mA, acceleration voltage of 400 V, incident angle of 5°, neutralizing beam current of 400 mA, neutralizing gas flow rate of 7 sccm, ion beam diameter of 150 mm, and etching rate of 0.0277 nm/s; each thinning process lasted 720 seconds, with an etching depth of 20 nm. The SEM (Zeiss, Gemini 300) parameters used were: acceleration voltage of 6 kV, stage bias voltage -5KV, aBSD detector, pixel size of 4 nm, and dwell time of 300 ns.

Cortex of rat spanning all cortical layers

The sample from cortex of a rat spanning all cortical layers was sectioned. 150 sections with 100 nm thickness and 3 mm×3 mm size were collected on five Si pieces (Supplementary Fig. 9a). Then the Si pieces were processed in the electron irradiation device (Bio-eBeam, China) to improve the conductivity of biological sections. After five PIB-SEM cycles were performed, these sections are almost etched away (Supplementary Fig. 9b). The PIB parameters used were as follows: ion beam energy of 80V, ion beam current of 100 mA, acceleration voltage of 400V, incident angle of 5°, neutralizing beam current of 400 mA, neutralizing gas flow rate of 7 sccm, ion beam diameter of 150 mm, etching rate of 0.0277 nm/s; each thinning process lasted 720 seconds, with an etching

depth of 20 nm. The SEM (Zeiss, Gemini 300) parameters used were: acceleration voltage of 6 kV, stage bias voltage -5KV, aBSD detector, pixel size of 10 nm, and dwell time of 300 ns.

Serial sections alignment

During the coarse alignment process, images of the stacks were down-sampled by 32X. We first performed pairwise alignment between every two adjacent images, extracted the corresponding points and applied affine transformations to estimate their deformations. In pairwise alignment, the sift method [17] was used to extract feature points of images, and the RANSAC [18] algorithm was used to filter corresponding point pairs. After pairwise alignment, we propagated the linear deformations across the entire stack [19]. In fine alignment process, we used an unsupervised optical flow network [20] to measure feature similarity between adjacent images. The optical flow network was then employed to estimate and compensate for cumulative registration error, thereby allowing for the reconstruction of the structure of biological tissues.

Evaluation of thinning uniformity across 4-inch wafer

To assess the thinning uniformity of PIB across 4-inch wafer, five ribbons of consecutive sections with 100 nm thickness were collected on Si pieces separately. The Si pieces were mounted on the different positions of a 4-inch wafer using conductive tape, and labeled as Si1 to Si5(see Supplementary Fig. 3a). The first five sections in each ribbon were selected for thickness measurement.

The original thickness of each section was measured using Atomic Force Microscopy (AFM) and recorded in Supplementary Table 1, which varied from 80 nm to 110 nm. These sections were then processed in the electron irradiation device to improve the conductivity. After that, the thickness of each section was measured again using AFM (Supplementary Table 1). It was worth noting that electron beam irradiation, due to the negligible mass of electrons, did not produce milling effects but resulted in a thickness reduction of approximately 20 % to 30 %.

All of sections in 4-inch wafer underwent three thinning processes with 20 nm thickness. After each thinning process, the section thickness was measured and the thickness of removed sample was recorded in Supplementary Table 2. Considering the reduction of section thickness caused by electron irradiation step, we calculated the compensated thickness *ac_ibe* for removed sample by

$$ac_ibe1 = (a - pi) *(m_ibe1/ pi) + m_ibe1$$
$$ac_ibe2 = (a - pi) *(m_ibe2/ pi) + m_ibe2$$
$$ac_ibe3 = (a - pi) *(m_ibe3/ pi) + m_ibe3$$

where *a* and *pi* were original and post-irradiation section thickness in Supplementary Table 1, *m_ibe* was the thickness of removed sample in Supplementary Table 2, the result of *ac_ibe* was detailed in Supplementary Table 3.

The results in Supplementary Table 3 indicate that the averaged thickness of removed sample at the center of the wafer deviates from the preset value by less than 0.17 nm, while at the wafer edge the deviation is less than 4.29 nm (see Supplementary Fig. 3b).

CPC and SSIM as continuity indicators

In order to evaluate the axial continuity of the volume data, we used chunked pearson correlation coefficient (CPC) [14] and structural similarity index measure (SSIM) [15] as evaluation indicators. CPC is used to evaluate the correlation between two images in the local (block) area, while SSIM

is used to measure the structural similarity of the two images. The aligned images in the datasets are evenly divided into image chunks without overlapping, as performed in [14]. The image chunks at the same horizontal position in adjacent sections are defined as matching pairs. The resolution of the input image was down-sampled to approximately $30 \times 30\ nm^2/pixel$, and each image chunk has a size of 64 × 64, which corresponds to a region of approximately $2 \times 2\ \mu m^2$. Following the chunk division process, these criteria were computed for each matching pair independently.

The CPC and SSIM values (Supplementary Fig. 7b) of the PIB-SEM dataset are mainly concentrated in the high-value range (CPC > 0.64, SSIM > 0.57), indicating good continuity along axial direction. The CPC values of the ATUM-SEM dataset are concentrated around 0.468, which is significantly lower. The distribution of SSIM criteria also exhibits a similar trend.

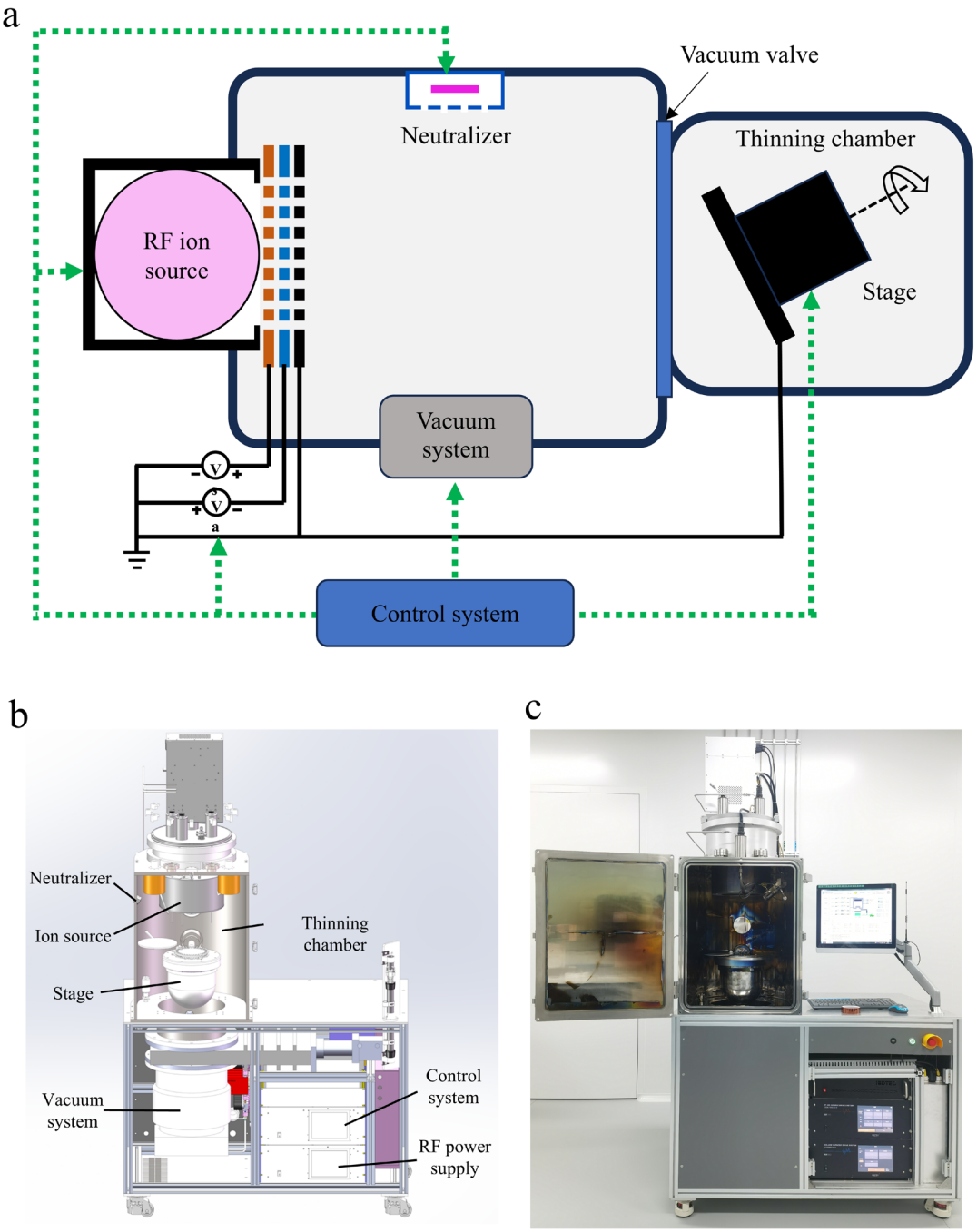

Supplementary Fig. 1. PIB prototype system. a, Operational mechanism of the PIB prototype. The parallel ion beam is emitted from the ion source. During the ion beam thinning process, to prevent the accumulation of positive charge (such as Ar^+ ions) on the sample surface, which could affect the uniformity of the thinning, an equal number of electrons are released through the neutralizer to neutralize the surface charge in real-time, ensuring the stability of the thinning process. The control system is responsible for coordinating the operation of each module. **b, c,** 3D model and actual appearance of the PIB prototype.

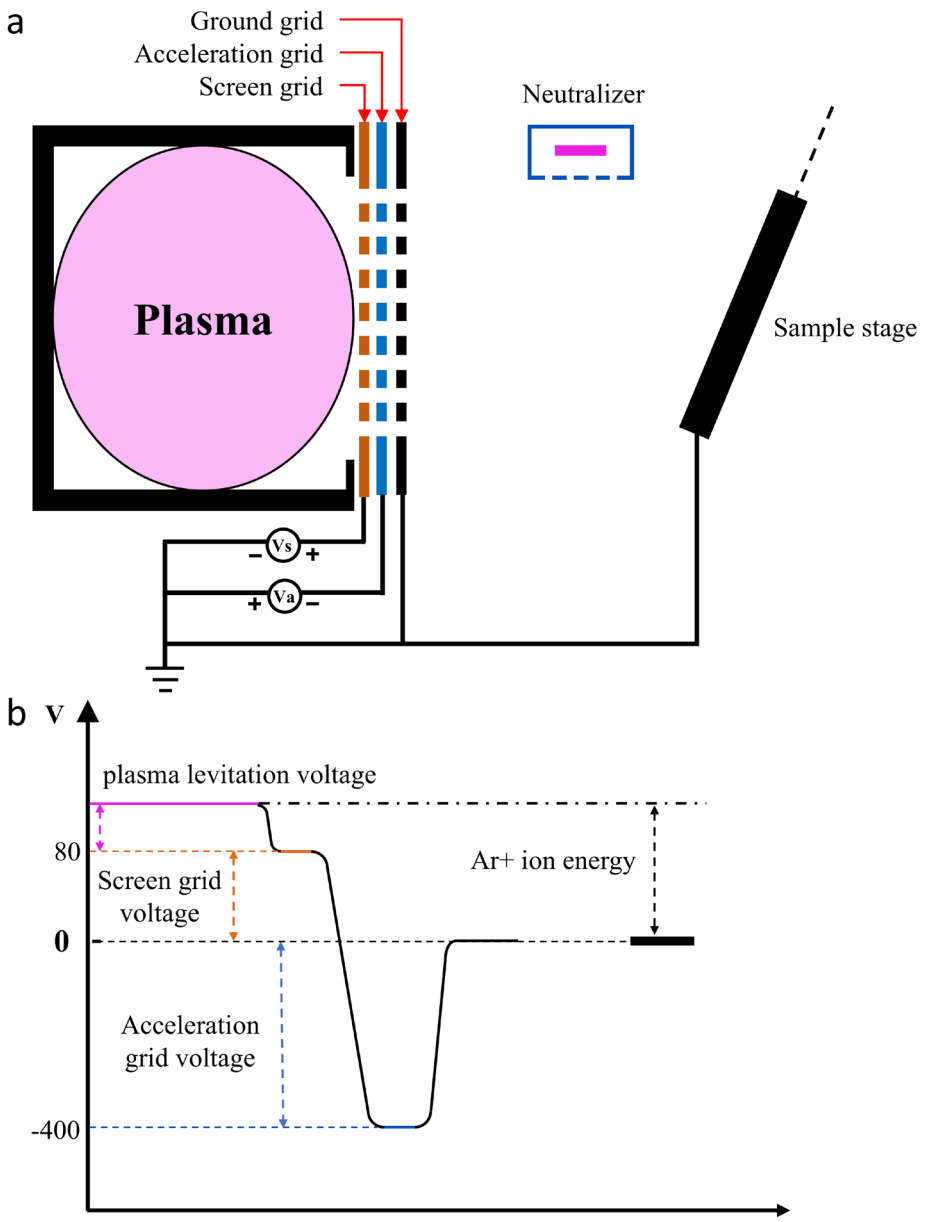

Supplementary Fig. 2. Ion source system. a, The ion source consists of a plasma chamber and a three-grid structure (screen grid, acceleration grid and ground grid). **b,** Electric potential diagram of three-grid structure. In the plasma chamber of the ion source, high-energy electrons collide with argon gas molecules through radio frequency (RF) excitation, causing ionization of the argon molecules and generating a large number of free electrons and Ar+ ions, thereby forming a plasma. Under the negative voltage (80V) applied to the screen grid, the Ar+ ions are extracted from the plasma chamber, while the electrons are shielded within the plasma, reducing interference from low-energy electrons in the ion beam and ensuring the purity of the ion beam. The ion beam is then shaped by an acceleration grid (400V) to achieve high uniformity and collimation. The coordination between the acceleration grid and the ground grid is only used for shaping the ion beam and does not alter its energy.

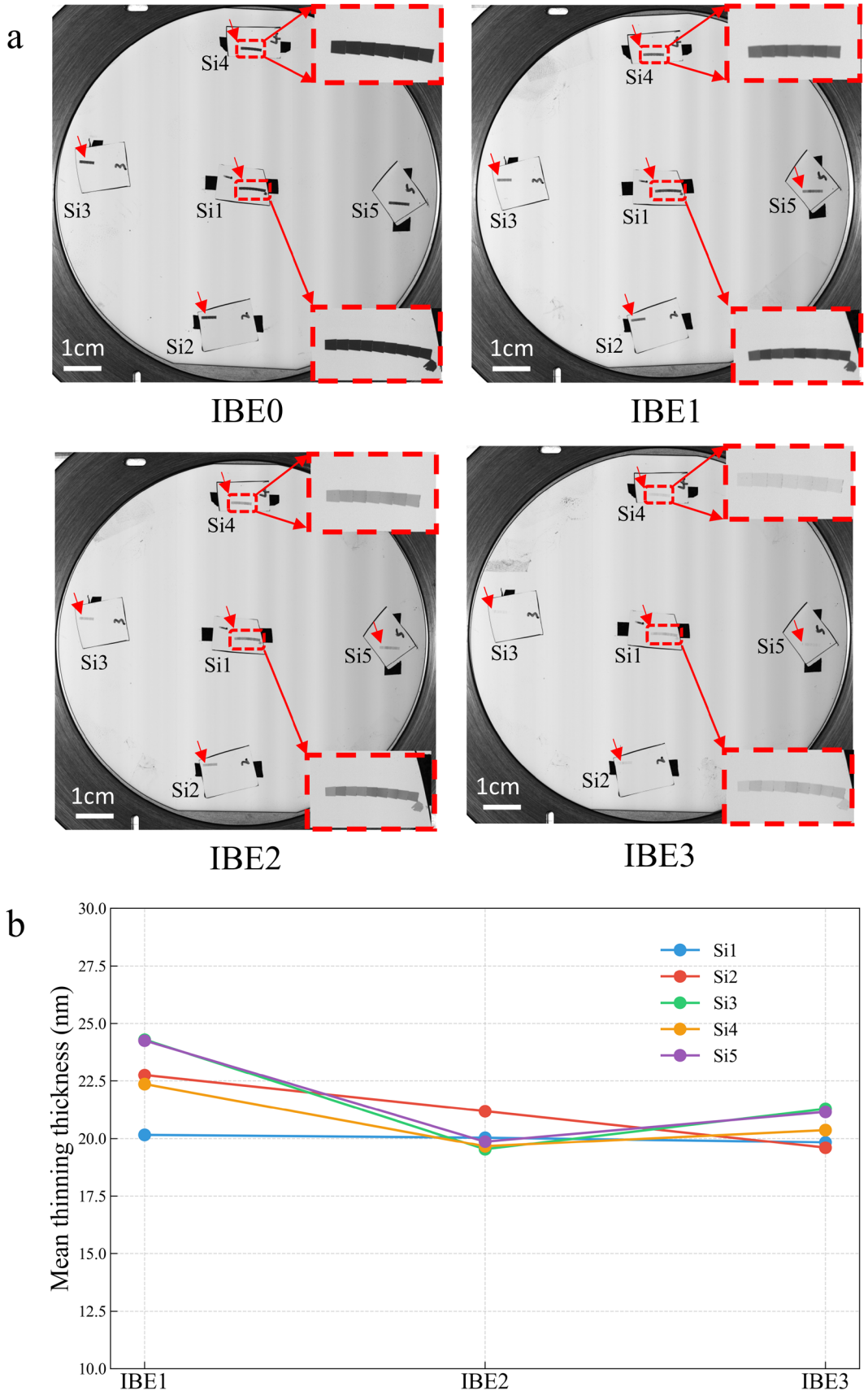

Supplementary Fig. 3. Evaluation of PIB thinning uniformity across 4-inch Si wafer. a, Five

Si pieces (labeled Si1 to Si5) are mounted on the different positions of a 4-inch wafer. Each Si piece contains 5–9 sections, which are marked by red arrows. IBE0 shows the wafer before thinning. IBE 1, IBE2, and IBE3 correspond to the wafer after the first, second, and third PIB thinning, respectively. The thicknesses of the first five sections (arranged from right to left) on each Si piece are measured with AFM. **b**, the mean of the compensated thickness for removed sample on the Si pieces after each thing process.

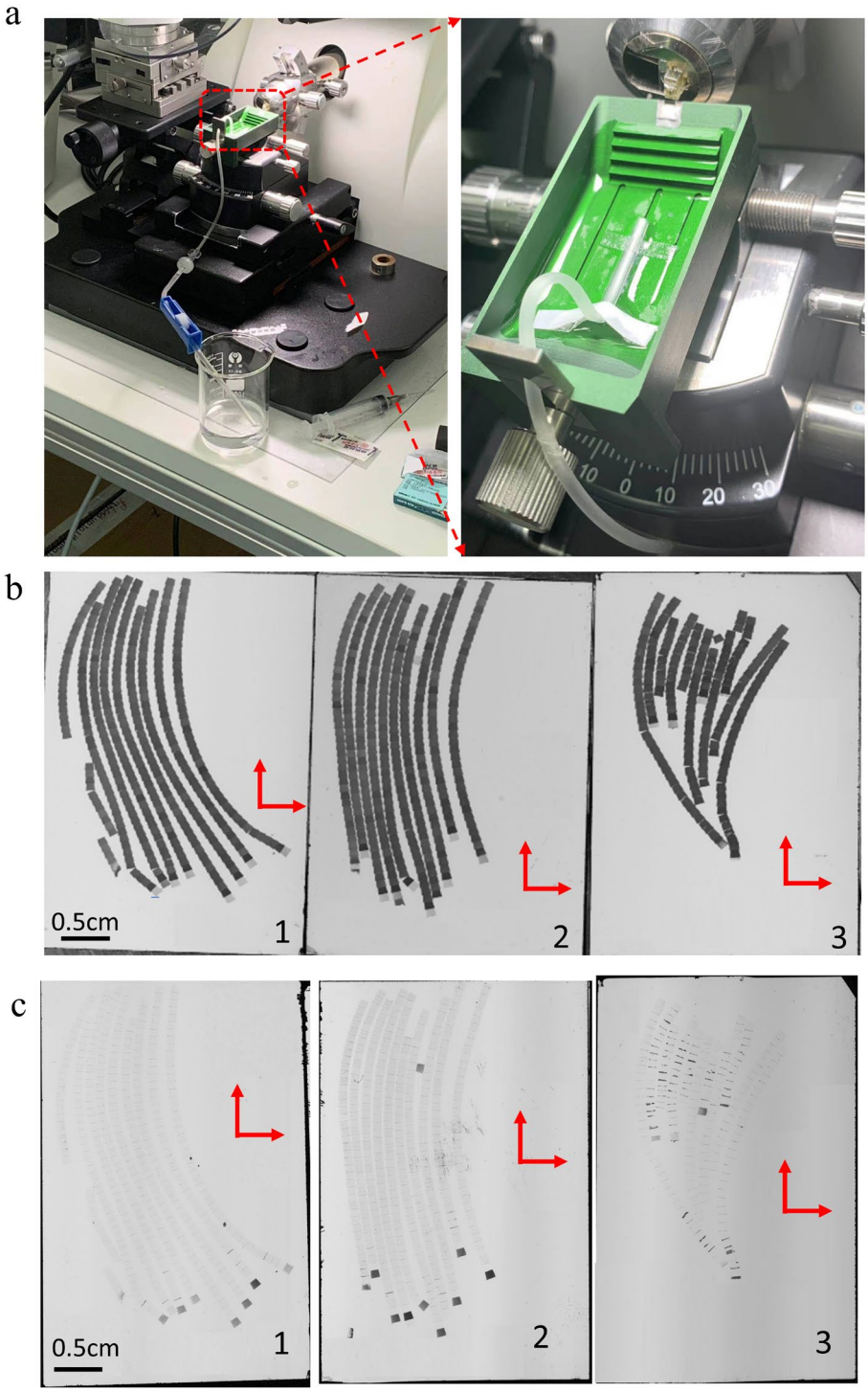

Supplementary Fig.4. Serial sections collection. a, A custom-built device used for mounting ribbons of serial sections onto hydrophilized Si pieces. **b**, Images of Si pieces before PIB thinning. The sample from prefrontal cortex of a rat is sectioned using an ultramicrotome, resulting in 1018 section with 100 nm thickness. The sections are collected onto three Si pieces. **c**, Image of Si pieces after five PIB thinning process.

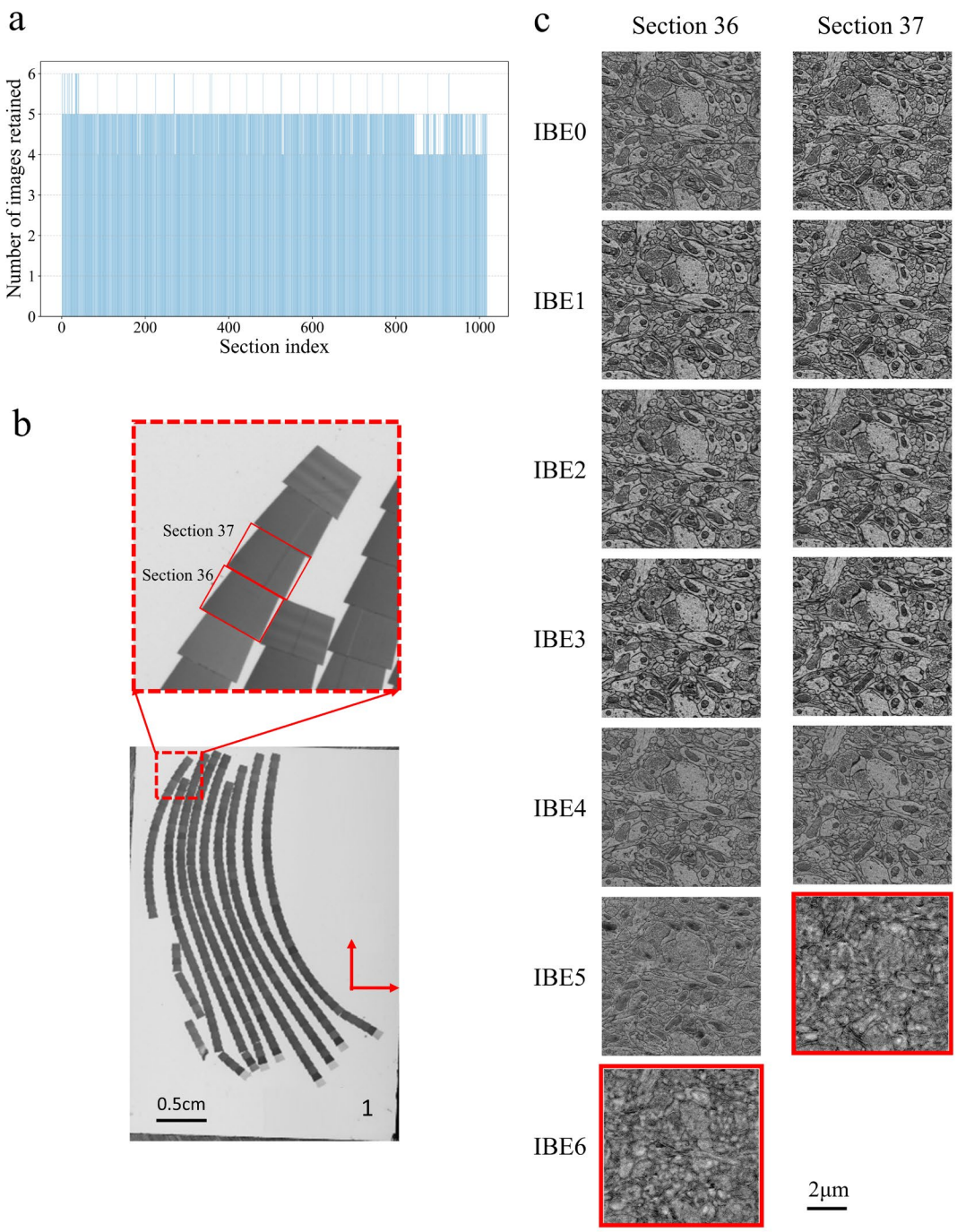

Supplementary Fig. 5. Number of images retained for each section. a, Number of images retained for each of the 1018 sections (see Supplementary Fig. 4b) after complete PIB thinning. **b**, Section 36 and 37 on the Si piece. **c**, SEM images of two consecutive sections (36 and 37) after multiple PIB thinning steps (20 nm thinning each). The red-boxed image shows that no meaningful content was left after complete thinning.

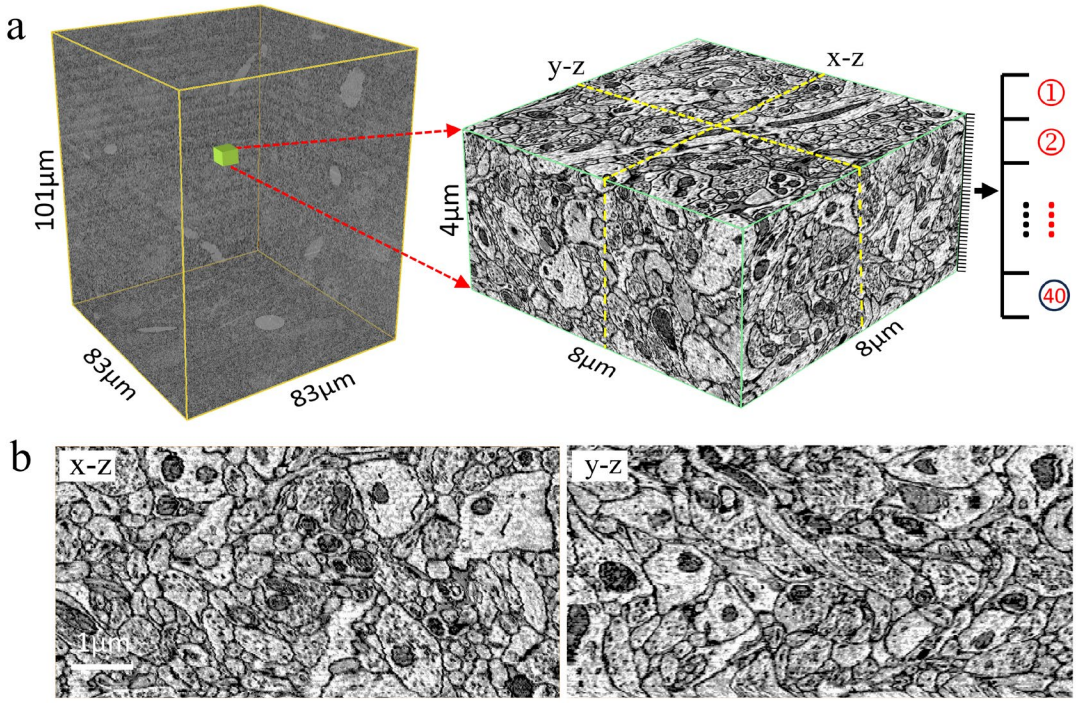

Supplementary Fig. 6. Image volume of prefrontal cortex of a rat. a, PIB-SEM volume (83 μm × 83 μm × 101 μm) spanning 1018 consecutive sections, and a sub-volume (8μm × 8μm × 4μm) spanning 40 consecutive sections. **b**, The x-z and y-z views of the yellow dashed line position in the sub-volume.

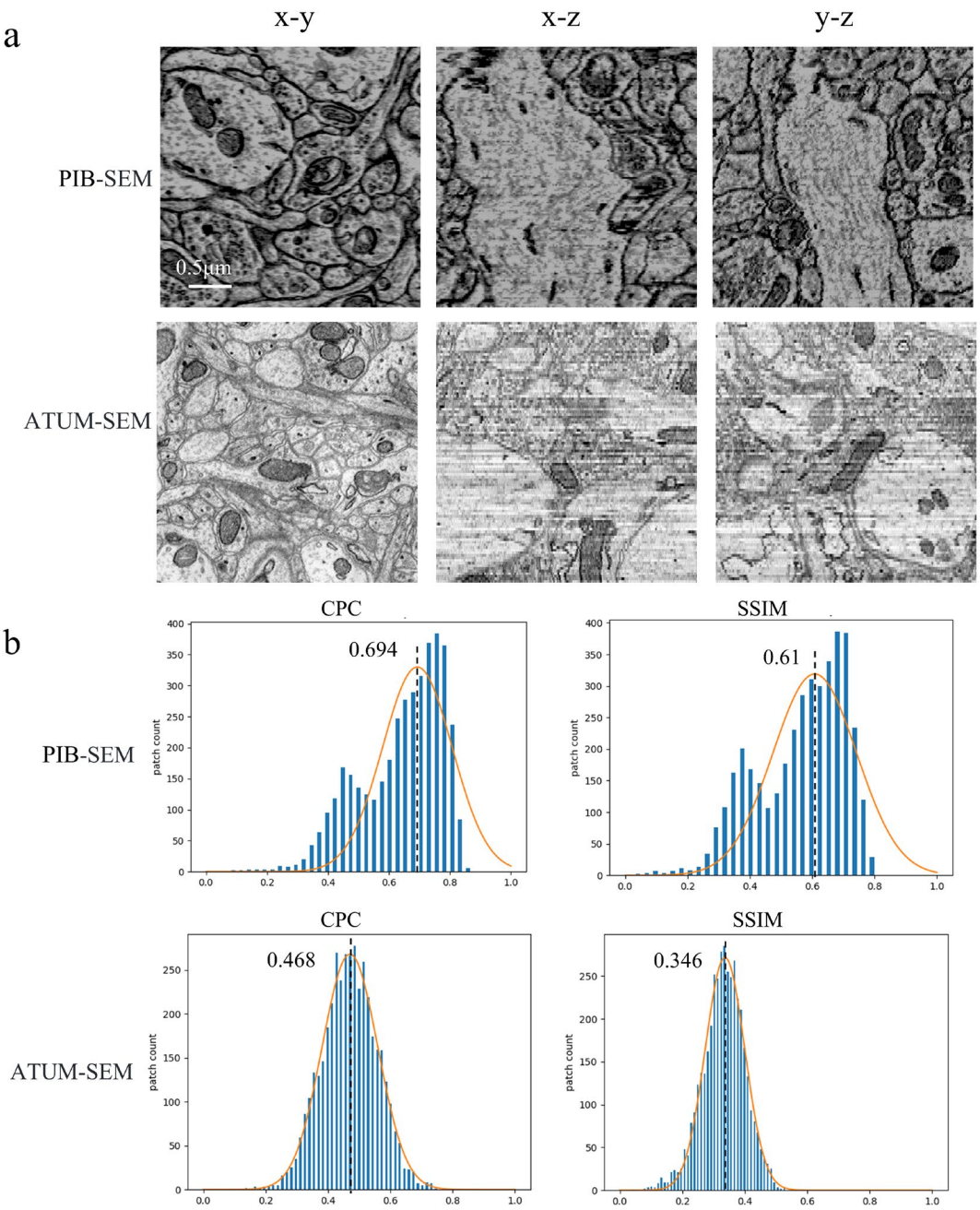

Supplementary Fig. 7. Comparison of different imaging volumes between the PIB-SEM volume (4 × 4 × 20 nm³ voxel) and the ATUM-SEM volume (3 × 3 × 30 nm³ voxel).

a, Qualitative comparison of x-y, x-z, and y-z views. Compared to the ATUM-SEM volume, the neuronal membrane structures in the PIB-SEM volumes exhibit better continuity and are more easily identifiable across all three views. In the x-z and y-z views, synaptic vesicles are distinguishable in the PIB-SEM volume but blurred in the ATUM-SEM volume. Scale bar: 0.5 μm. **b**, Evaluation of z-axial continuity using CPC and SSIM. The brown line represents the Gaussian distribution fitting curve of the histogram. The value indicates the peak coordinate of the Gaussian distribution.

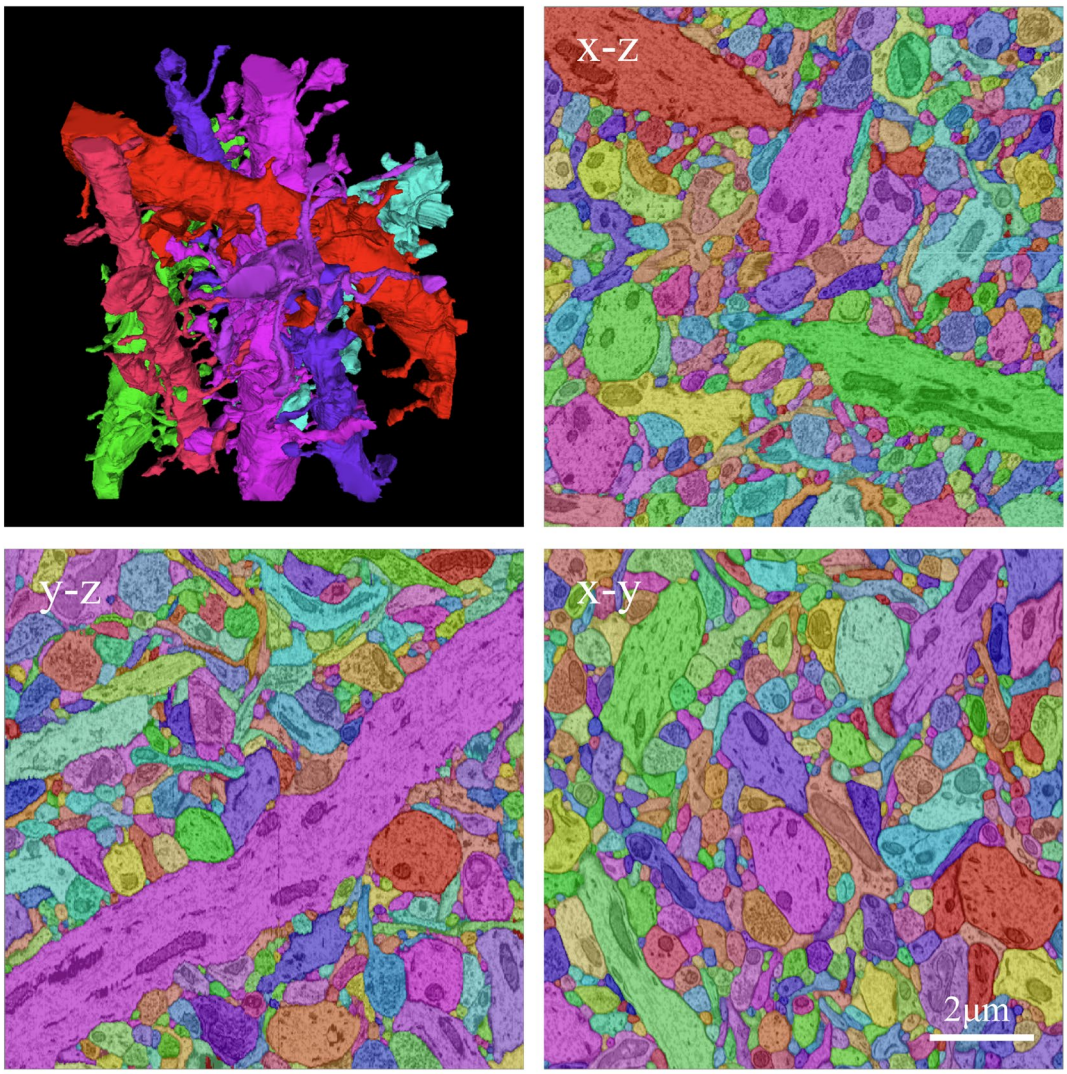

Supplementary Fig. 8. 3D segmentation of a PIB-SEM volume. Dendritic reconstruction of the PIB-SEM volume (10 μm × 10 μm × 10 μm) and the x-z, x-y, and y-z views of the volume segmentation results.

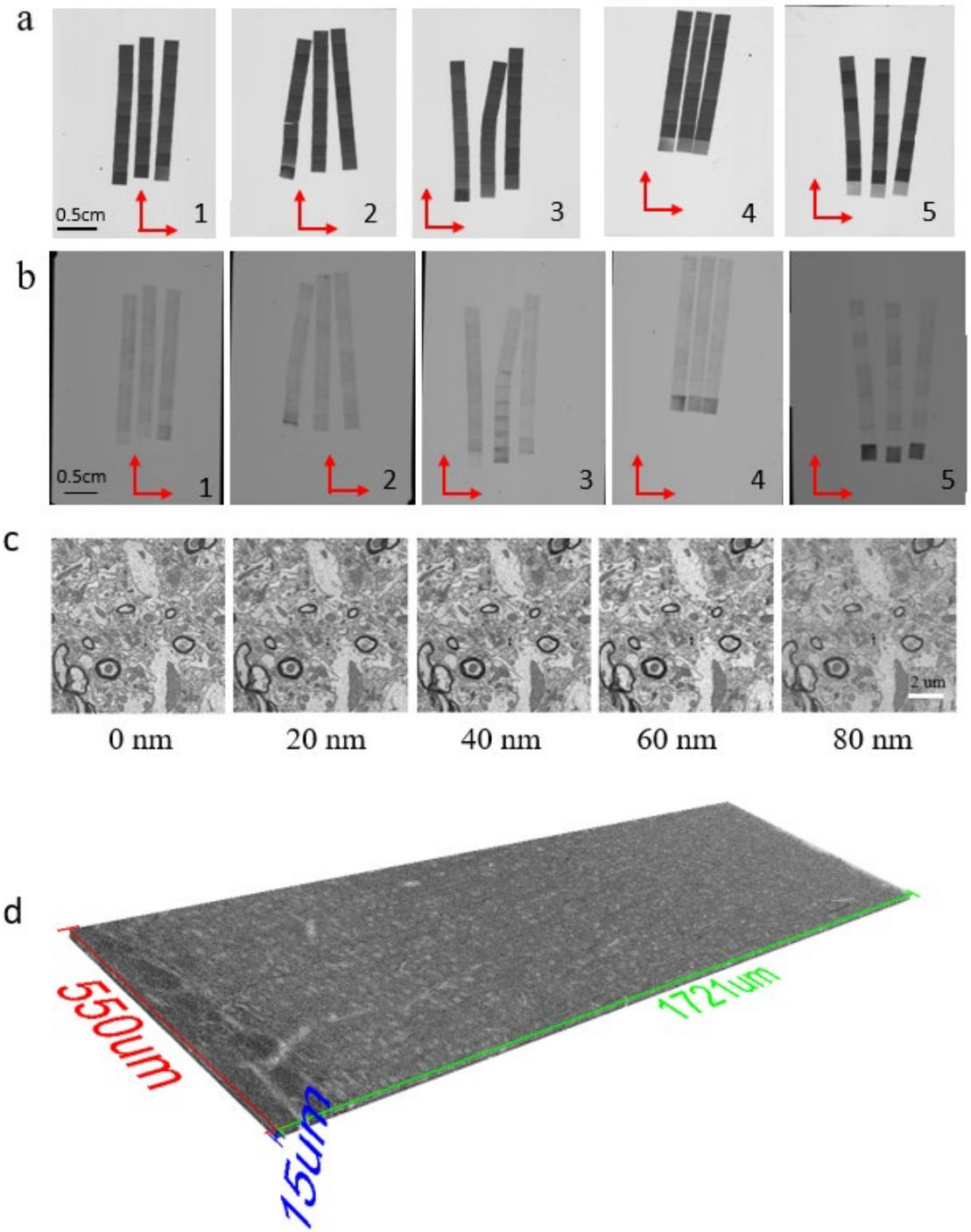

Supplementary Fig. 9. Image volume of cortex of rat spanning all cortical layers. a, 150 serial sections with 100 nm thickness are collected on five Si pieces. **b**, Image of Si pieces after five PIB thinning process. **c,** SEM images of a section after each PIB thinning process. **d,** Stitched stack of 1721 μm × 550 μm × 15 μm PIB-SEM volume.

Supplementary Table 1. Thickness (nm) of sections on each Si piece before and after electron irradiation.

	Si num	Section1 thickness	Section2 thickness	Section3 thickness	Section4 thickness	Section5 thickness
Original (*a*)	Si1	108.12	108.76	102.43	115.24	109.21
	Si2	92.98	91.30	95.66	91.51	85.26
	Si3	82.80	80.45	82.25	84.13	81.05
	Si4	91.78	97.79	91.70	99.86	98.15
	Si5	84.96	87.78	89.00	91.87	96.17
post-Irradiation (*pi*)	Si1	76.38	75.61	71.12	82.42	76.91
	Si2	69.93	69.94	70.11	68.86	64.25
	Si3	60.22	56.78	58.99	61.63	58.00
	Si4	67.20	68.81	66.48	70.71	69.21
	Si5	64.69	67.10	68.53	70.45	74.34

Supplementary Table 2. Thickness (nm) of removed sample after each PIB thinning.

	Si num	Section1 thickness	Section2 thickness	Section3 thickness	Section4 thickness	Section5 thickness
IBE1 (*m_ibe1*)	Si1	14.74	13.47	14.38	15.39	12.90
	Si2	17.93	15.52	16.11	17.76	18.14
	Si3	16.06	17.36	16.36	19.29	18.38
	Si4	16.01	14.26	13.85	19.13	16.61
	Si5	19.65	18.08	18.8	17.21	19.29
IBE2 (*m_ibe2*)	Si1	14.17	14.52	12.91	14.32	14.51
	Si2	14.50	17.62	14.98	14.45	18.11
	Si3	14.29	13.92	14.33	11.88	15.81
	Si4	14.06	12.07	16.53	13.78	13.88
	Si5	14.55	13.85	15.20	16.53	16.08
IBE3 (*m_ibe3*)	Si1	13.48	12.38	16.68	15.66	11.51
	Si2	13.98	14.47	17.71	15.62	11.75
	Si3	13.46	14.53	14.78	18.02	15.83
	Si4	14.07	17.16	13.54	15.26	12.69
	Si5	15.59	16.58	15.77	16.52	16.70

Supplementary Table 3. Compensated thickness (nm) of removed sample after each PIB thinning.

	Si num	Section1 thickness	Section2 thickness	Section3 thickness	Section4 thickness	Section5 thickness
IBE1 (*ac_ibe1*)	Si1	20.86	19.37	20.72	21.53	18.32
	Si2	23.84	20.26	21.99	23.61	24.08
	Si3	22.08	24.59	22.8	26.32	25.68
	Si4	21.87	20.27	19.11	27.02	23.55
	Si5	25.81	23.65	24.41	22.44	24.96
IBE2 (*ac_ibe2*)	Si1	20.06	20.89	18.60	20.03	20.61
	Si2	19.28	23.00	20.43	19.20	24.03
	Si3	19.64	19.73	19.98	16.22	22.10
	Si4	19.20	17.15	22.8	19.47	19.68
	Si5	19.11	18.12	19.73	21.55	20.81
IBE3 (*ac_ibe3*)	Si1	19.08	17.81	24.03	21.90	16.35
	Si2	18.59	18.89	24.17	20.76	15.60
	Si3	18.51	20.59	20.61	24.60	22.12
	Si4	19.22	24.38	18.67	21.55	18.00
	Si5	20.48	21.69	20.48	21.54	21.60

References

[1] T. A. Jarrell *et al.*, "The connectome of a decision-making neural network," *science,* vol. 337, no. 6093, pp. 437-444, 2012.

[2] M. Zhen and A. D. Samuel, "C. elegans locomotion: small circuits, complex functions," *Current opinion in neurobiology,* vol. 33, pp. 117-126, 2015.

[3] T. Ohyama *et al.*, "A multilevel multimodal circuit enhances action selection in Drosophila," *Nature,* vol. 520, no. 7549, pp. 633-639, 2015.

[4] J. Ngai, "BRAIN 2.0: Transforming neuroscience," *Cell,* vol. 185, no. 1, pp. 4-8, 2022.

[5] D. Witvliet *et al.*, "Connectomes across development reveal principles of brain maturation," *Nature,* vol. 596, no. 7871, pp. 257-261, 2021.

[6] Z. Zheng *et al.*, "A complete electron microscopy volume of the brain of adult Drosophila melanogaster," *Cell,* vol. 174, no. 3, pp. 730-743. e22, 2018.

[7] M. Winding *et al.*, "The connectome of an insect brain," *Science,* vol. 379, no. 6636, p. eadd9330, 2023, doi: 10.1101/2022.11.28.516756.

[8] A. Motta *et al.*, "Dense connectomic reconstruction in layer 4 of the somatosensory cortex," *Science,* vol. 366, no. 6469, p. eaay3134, 2019.

[9] J. Kornfeld and W. Denk, "Progress and remaining challenges in high-throughput volume electron microscopy," *Current opinion in neurobiology,* vol. 50, pp. 261-267, 2018.

[10] J. S. Phelps *et al.*, "Reconstruction of motor control circuits in adult Drosophila using automated transmission electron microscopy," *Cell,* vol. 184, no. 3, pp. 759-774. e18, 2021.

[11] C. S. Xu, S. Pang, K. J. Hayworth, and H. F. Hess, "Enabling FIB-SEM systems for large volume connectomics and cell biology," *bioRxiv,* p. 852863, 2019.

[12] K. J. Hayworth *et al.*, "Gas cluster ion beam SEM for imaging of large tissue samples with 10 nm isotropic resolution," *Nature methods,* vol. 17, no. 1, pp. 68-71, Jan. 2020, doi: 10.1038/s41592-019-0641-2

[13] N. Kasthuri *et al.*, "Saturated reconstruction of a volume of neocortex," *Cell,* vol. 162, no. 3, pp. 648-661, 2015.

[14] S. Popovych *et al.*, "Petascale pipeline for precise alignment of images from serial section electron microscopy," *Nature communications,* vol. 15, no. 1, p. 289, 2024.

[15] Z. Wang, A. C. Bovik, H. R. Sheikh, and E. P. Simoncelli, "Image quality assessment: from error visibility to structural similarity," *IEEE transactions on image processing,* vol. 13, no. 4, pp. 600-612, 2004.

[16] Y. Zhang, J. Guo, H. Zhai, J. Liu, and H. Han, "Segneuron: 3d neuron instance segmentation in any em volume with a generalist model," in *International Conference on Medical Image Computing and Computer-Assisted Intervention*, 2024: Springer, pp. 589-600.

[17] D. G. Lowe, "Distinctive image features from scale-invariant keypoints," *International journal of computer vision,* vol. 60, no. 2, pp. 91-110, 2004.

[18] M. FISCHLER AND, "Random sample consensus: a paradigm for model fitting with applications to image analysis and automated cartography," *Commun. ACM,* vol. 24, no. 6, pp. 381-395, 1981.

[19] Y. Lv, X. Chen, C. Shu, and H. Han, "Robust global optimized affine registration method for microscopic images of biological tissue," in *ICASSP 2020-2020 IEEE International Conference on Acoustics, Speech and Signal Processing (ICASSP)*, 2020: IEEE, pp. 1070-1074.

[20] T. Xin *et al.*, "A novel registration method for long-serial section images of EM with a serial split technique based on unsupervised optical flow network," *Bioinformatics,* vol. 39, no. 8, p. btad436, 2023.